

Production, Crystallization, and Raman Shifting with *para*-Hydrogen

By

Lauren E. Moore

Thesis
for the
Degree of Bachelor of Science
in
Chemistry

College of Liberal Arts and Sciences
University of Illinois
Urbana-Champaign, Illinois

2010

Table of Contents

Chapter 1: <i>Para</i>-Hydrogen Converter	2
1.1 Theory	2
1.2 Re-design	3
1.3 Set-up	4
1.4 Production of <i>para</i> -Hydrogen	7
1.5 Enrichment determination	9
1.5.1 NMR	9
1.5.2 Thermal conductance	11
Chapter 2: Refractive Index of Solid <i>para</i>-Hydrogen	14
2.1 Theory	14
2.2 Design	16
2.3 Crystal production	18
2.4 How to determine the index	19
2.5 Results	22
2.6 Discussion	24
Chapter 3: Raman Laser Design	28
3.1 Theory	28
3.2 Requirements	32
3.3 Initial Design	34
3.4 Conclusion	38
References	39
Appendix A: Refractive Index Derivation	42
Appendix B: Brewster's Angles	45

Chapter 1

para-Hydrogen Converter

1.1 Theory

Hydrogen is the most abundant element in the universe and molecular hydrogen can exist in two separate states, *ortho*-hydrogen and *para*-hydrogen. *Ortho*-hydrogen represents a symmetrically aligned spin orientation ($I=1$), while *para*-hydrogen exists with an anti-aligned spin orientation ($I=0$). In normal hydrogen, the ratio of *ortho*: *para* is about 3:1. Hydrogen has been an important element for the study of quantum mechanics because it can be easily fit to an ideal system. The two separate states of hydrogen were first theoretically proposed by Heisenburg and Hund in 1927 [1] and later experimentally discovered by Bonhoeffer [2].

Without an external magnetic field, the conversion from *ortho*-hydrogen to *para*-hydrogen is extremely slow and negligible at room temperature conditions. This allows the two states to be treated as separate species under normal conditions. Wigner originally suggested a mechanism for the conversion of *ortho*-hydrogen to *para*-hydrogen involving magnetic conversion in a homogeneous phase [3]. There are now two different mechanisms generally accepted for the conversion [4]. The first involves dissociation of two or more hydrogen molecules and recombination of the hydrogen atoms with the spins anti-aligned, while the second is induced by an inhomogeneous magnetic field as a result of the paramagnetism of the unpaired electrons. Minaev and Ågren proposed a new mechanism more than two orders of magnitude stronger than the traditional inhomogeneous magnetic field [5]. This “spin catalysis” theory suggests that the excited-state hydrogen mixed into the ground state induces spin-uncoupling and removal of the antisymmetrization of the wave function. This removal results in

an effective Fermi contact hyperfine interaction between the *ortho*- and *para*- states, allowing for more rapid conversion between the two states.

Bonhoeffer and Hartek built the first device to convert *ortho*- to *para*- hydrogen in 1929, using activated charcoal as the catalyst and either liquid nitrogen or liquid helium to cool the system [2]. Higher enrichments of *para*-hydrogen were obtained using liquid helium rather than liquid nitrogen. Silvera explored the most efficient ways to convert *ortho*- to *para*- hydrogen [6]. Silvera understood that at low temperatures hydrogen could equilibrate to almost entirely *para*-hydrogen. However this process could take up to a week without the appropriate catalyst to speed the process. Different catalysts explored included ferric oxide and Apache nickel silica (manufactured by Houdry), both of which must be activated to work properly. Activation removes any water molecules from the surface of the catalyst. If left inactivated, the water molecules greatly reduce the surface area available for hydrogen absorption.

1.2 Re-design

Our *para*-hydrogen converter was originally designed and set-up by Tom [7]. In order to proceed with the solid hydrogen experiment (as described in Chapter 2), the optics table on which the converter rested needed to be utilized to set-up the optics required for this experiment. Thus, a table was built, using unistrut as support and wood as the table top, standing two feet above the current optics table. With the addition of this table, new constraints were imposed upon the converter system.

First, in order to operate the converter from the ground, all pressure gauges and valves needed to be easily operated and viewed. In order to quantify the *para*-hydrogen enrichment, the thermal conductance cell and NMR (nuclear magnetic resonance) attachment needed to be placed

so that they can both be easily operable from the ground. Lastly, with the addition of the solid hydrogen experiment, a line was needed to supply the *para*-hydrogen to the cryostat.

The new design is shown in Figure 1.1. There was a one inch diameter hole drilled into the wood table where $\frac{1}{4}$ " stainless steel tubing connects the converter lines to the thermal conductance cell and NMR attachment, which are suspended immediately above the optics table. *para*-Hydrogen can be stored in the large Teflon tank and then allowed to flow into these lines to measure the enrichment. Due to the precision required with the thermal conductance cell, this is an optimal arrangement for the operator.

When the set-up to produce a solid hydrogen crystal is functional, *para*-hydrogen will need to be fed to the cryostat either from a storage tank or directly from the converter. Thus, an additional line was attached that allowed access to either the tank or converter. This line ran across the table and connected directly to the components required to produce a crystal.

1.3 Set-up

The new set-up was modeled from the original design, but modifications were applied to fit the new requirements of the system, as noted in Section 1.2. Figure 1.1 shows a diagram of the new set-up. In order to produce >99.99% pure *para*-hydrogen, this system was modeled after the closed cycle ^4He cryostat developed by Tam and Fajardo [8]. Within the cryostat, copper tubing lined with ferric hydroxide makes up the coil section where conversion occurs. Figure 1.2 (adapted from Tom [9]) shows the overview of the converter and a close-up of the copper coil. Further information about the design, fabrication, and use of the cryostat is available in the EPAPS document [10] and from Tom [9]. Tam and Fajardo optimized the *para*-hydrogen conversion at a maximum rate of 0.12 SLM (standard liters per minute), while our current

cryostat can convert at an optimal rate up to 0.4 SLM [9]. This represents a significant improvement over the previous design.

The hydrogen generator (Parker Balston H2-1200) produces normal (25.07% *para*-) hydrogen at a rate controlled by the operator. The flow into the cryostat (Janis CCS-100/204 Optical 10K Refrigerator) is then regulated with a high purity stainless pressure regulator (Matheson Tri Gas 3433-NV-5, M63-2216). As shown in the diagram, there is a by-pass line that goes around the cryostat. This by-pass line is used to take normal hydrogen from the generator to use as a standard to confirm the enrichment of the *para*-hydrogen in the quantitative tests without passing through the converter. There is another high purity pressure gauge on the “out” line from the converter to verify the pressure of gas as it leaves the converter and fills the large storage tank. Both pressure gauges were placed next to each other, allowing the operator to compare both pressure readings at once. The converter temperature is monitored and controlled using a temperature controller (Lakeshore DRC-91C) with a silicon diode sensor. The toggles in the back of the controller should be set to “111” to ensure the proper temperature calibration curve. The design of the converter is thoroughly discussed by Tom [7, pg. 11-14].

The turbo pump (Pfeiffer TSH 071E) is used to evacuate the lines between runs to ensure the highest enrichment of *para*-hydrogen will be obtained. When producing a large amount of *para*-hydrogen, the hydrogen is stored in a Teflon-lined storage tank (Swagelok 304LHDF4-1GALC-T). This tank is used to reduce back conversion rates to about 1.7% per week [9]. Not shown in the diagram are the lines that connect to the thermal conductance cell and NMR attachment, which are beneath the raised tabletop. Throughout the set-up, stopcock valves (Swagelok SS-42GS4) are used to direct the flow of normal hydrogen upstream of the converter, and to direct the outflow of converted gas. All the stopcock valves (shown as rectangular pieces

in Figure 1.1) were placed within five inches of the edge of the table, so that the operator can easily open and close them while standing on the ground. Figure 1.3 shows a picture of the converter system in the laboratory.

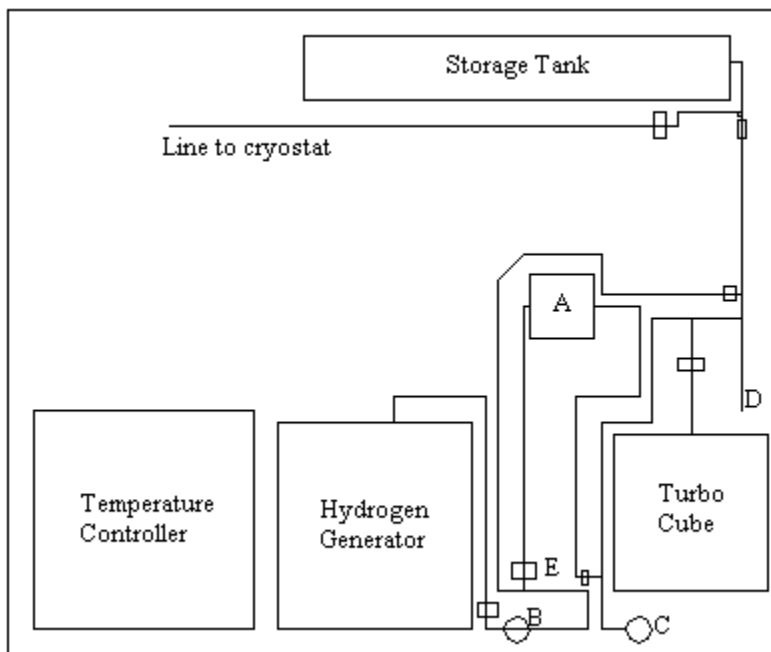


Figure 1.1: Diagram of *para*-hydrogen converter. A: *para*-hydrogen converter; B: “in” pressure gauge; C: “out” pressure gauge; D: line down to thermal conductance cell (Figure 1.2) and NMR attachment; E: stopcock valve.

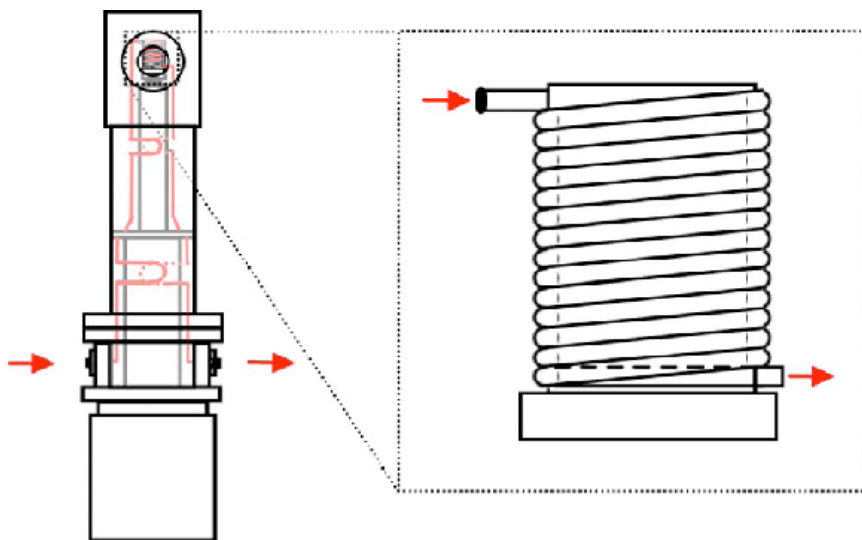


Figure 1.2: Drawing of *para*-hydrogen converter and close-up view of the copper coil containing the ferric hydroxide.

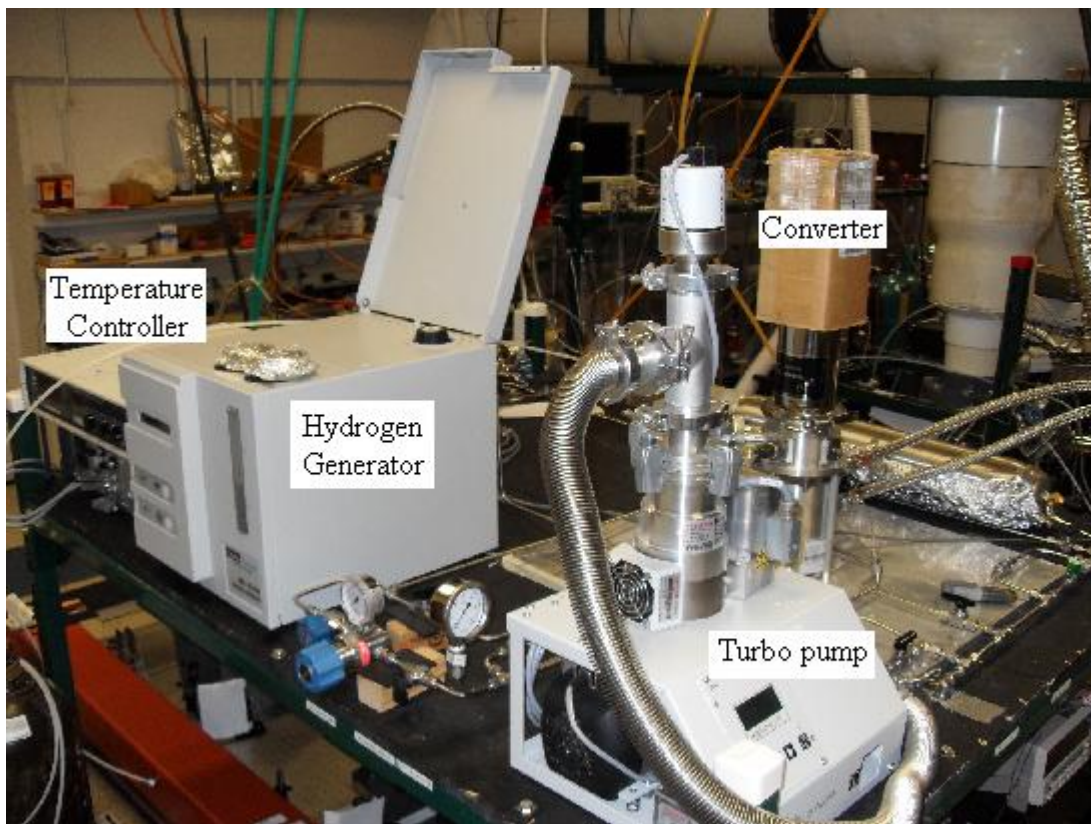


Figure 1.3: Picture of the converter system with important components labeled.

1.4 Production of *para*-Hydrogen

To produce the highest enrichment of *para*-hydrogen, compressed helium gas is used to cool the converter. With liquid nitrogen, the highest enrichment of *para*-hydrogen obtained is ~ 51%, while cooling to 20 K with liquid He can result in enrichment of ~99.8% [6]. In order to produce ~99.99% enriched *para*-hydrogen, the temperature of the converter is maintained at 14.0 K by heating the liquid helium. The turbo pump is used to evacuate the system completely before beginning, but the converter is not evacuated to avoid damaging the catalyst. Ensure that the chilled water loop is already open before the hydrogen generator is turned on. The Lakeshore temperature controller is connected to the cryostat in port B, set to 14.0 K, and the heater is set to “Max.” The calibration curve selected reads “111,” obtained by flipping the knobs in the back.

The converter will take approximately one hour to reach 14.0 K and another hour to stabilize. At this point, the tank and bypass line should be closed, and the turbo pump closed from the system and allowed to spin down. Normal hydrogen is slowly introduced into the converter with a backing pressure of 330 mbar. At this point, the line into and out of the converter is opened, and the pressure gauge into the converter is set to 0 psi. As this gas enters the converter, it undergoes a phase change to liquid hydrogen. Before the downstream pressure can increase, the entire coil must fill with liquid hydrogen. The downstream pressure will increase after the phase change is complete, and equilibrium between the pressure gauges will be reached. More normal hydrogen is run through the converter to remove any unconverted gas. The converter is closed off, and the entire system evacuated before continuing. It is important to keep the storage tank completely closed during this process.

Then, *para*-hydrogen production begins by increasing the pressure into the converter. The heater voltage is closely monitored during this process; a voltage lower than 3% may indicate that the flow rate is too great (causing a large thermal load from the warm hydrogen) and result in some hydrogen not being converted. A heater voltage too high (10% or more) can indicate that there is frozen hydrogen within the converter blocking the path for hydrogen gas. The difference between the upstream and downstream pressures is maintained 2-5 psi and can be increased for higher downstream pressures.

The *para*-hydrogen produced is stored in a one gallon Teflon storage tank and filled until a pressure of ~95 psig is reached on the downstream pressure gauge. A Teflon storage tank was shown to produce a lower back conversion rate than an aluminum storage tank [9]. Impurities in the storage tank can increase the back conversion rate, so the tank must be evacuated overnight before allowing any *para*-hydrogen to enter. After the preparation of *para*-hydrogen is complete,

the temperature of the cryostat must be closely monitored. Liquid hydrogen will become a gas at 31 K, which can create high pressure inside the cryostat. The cryostat should be vented properly by never opening directly to the pump or the atmosphere before reaching room temperature. To do this, the line out of the converter is opened to the lines to release any pressure build-up. Once the pressure equilibrates, the line out of the converter is closed off. The pressure in the lines is vented to atmosphere. The turbo pump is then turned on and allowed to evacuate the lines to around 10^{-2} mbar before being closed off from the system. The process repeats from the beginning until above 32 K, and no pressure is built-up in the converter.

1.5 Enrichment determination

After successfully producing a batch of *para*-hydrogen, the enrichment is determined using NMR and thermal conductance analysis. These methods can be used together to compare results or alone if time is short.

1.5.1 NMR

A spinning, charged nucleus creates a magnetic field when interacted with an electromagnetic pulse. As the nuclei relax, a time-domain radio-frequency signal, called the free induction decay (FID), is detected. With this signal, a Fourier transform can be applied to transform the measurement into the frequency domain [11]. *Ortho*-hydrogen has a net magnetic moment that can be detected using NMR and quantified by integrating the Fourier transformed FID. On the other hand, *para*-hydrogen produces no net magnetic field and cannot be aligned with a strong magnetic field, thus producing no signal, or FID. This theory can be used to

quantify the presence of *para*-hydrogen when an unknown sample is compared to a normal hydrogen sample.

To collect the hydrogen sample, glass NMR tubes (Wilmad Lab Glass 528-PV-7) were fit with J. Young valves to ensure a good seal. J. Young valves allow for easy attachment of the NMR tube to the vacuum system while preventing any air from entering the sample tube. The introduction of oxygen to the tubes can increase the back conversion rate to *ortho*-hydrogen. The tube is filled with 20-40 psi of the newly converted *para*-hydrogen gas, while a sample of normal hydrogen is also collected with the same pressure. TMS (tetramethylsilane) was previously added to help shim the NMR magnet and standardize the samples. However, higher back conversion rates were measured when TMS was introduced into the *para*-hydrogen environment [9]. We discovered that we could accurately determine the *para*-hydrogen concentration without shimming the magnet, so TMS is no longer used in the procedure. Figures 1.4 a and b show a comparison between a normal hydrogen sample and an enriched *para*-hydrogen sample.

After filling a NMR tube, measurements were taken as quickly as possible (within ten minutes) to reduce the effects of back conversion using a Varian Unity Inova 500 Narrow Bore NMR spectrometer. The peaks were integrated using Igor Pro 5.03 to determine the intensity of each peak. Since the amount of *para*-hydrogen in the normal hydrogen sample is known, the amount of *para*-hydrogen in the newly converted sample is easily determined by comparing the intensity of each integrated peak.

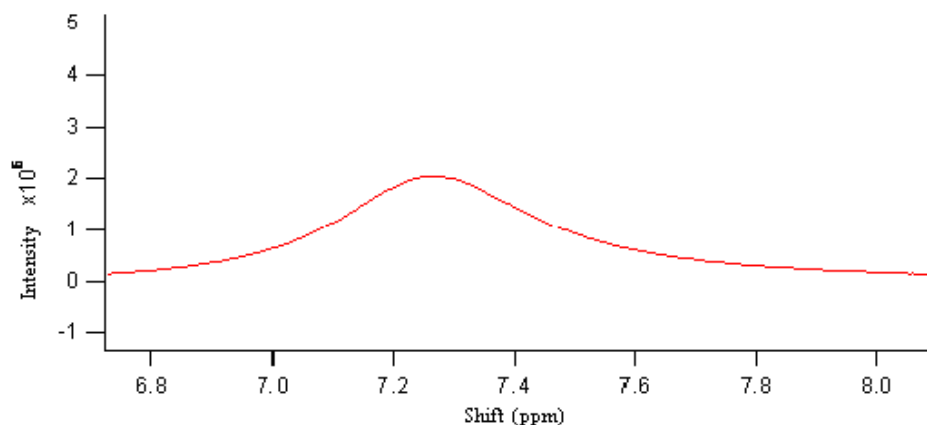


Figure 1.4a: Normal hydrogen sample peak from the NMR (75% *ortho*-).

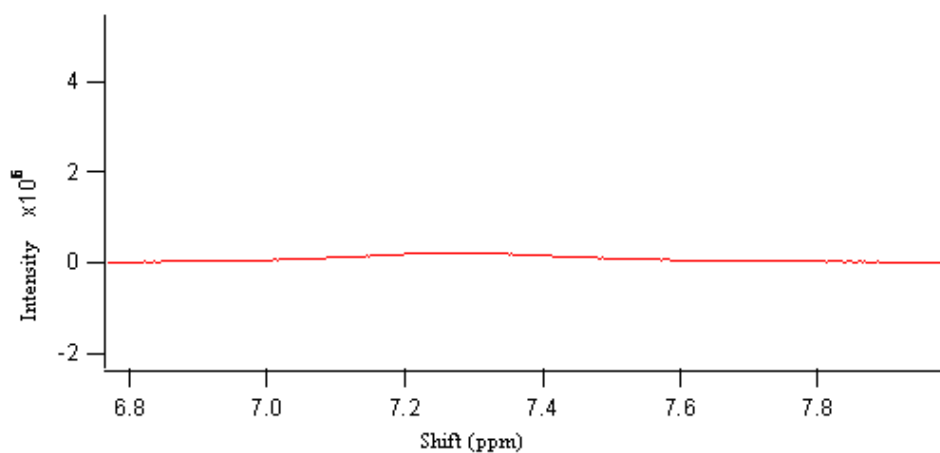


Figure 1.4b: Enriched *para*-hydrogen sample from the NMR (~10% *ortho*-).

1.5.2 Thermal conductance

Thermal conductance utilizes the fact that *para*-hydrogen consists of only even rotational states, while *ortho*-hydrogen consists of only odd rotational states. This results in different thermal conductivities. By using resistive heating, a tungsten wire in a liquid nitrogen cooled cell is filled with hydrogen gas and maintained at 175 K, the temperature that displays the greatest difference in thermal conductivity between the two states. Resistive heating involves passing an

electric current through the wire to produce thermal heat. The resistance in the tungsten wire will change according to Equation 1.1.

$$R = R_0(1 + \alpha\Delta T) \quad (1.1)$$

R_0 is the resistance of the filament at a known temperature (usually close to 300K), α is its thermal resistance coefficient ($4.9 \times 10^{-3} \text{ K}^{-1}$ for tungsten), and ΔT is the temperature change [12, pg. 114]. Since *para*-hydrogen has a higher thermal conductivity, it will result in a cooler wire and lower resistance at a given current.

Our thermal conductance cell was modeled after Farkas [13, pg. 20-28] and Steward [14]. Figure 1.5 shows the design of the thermal conductance cell. The design was updated from Farkas and Steward with stainless steel flanges and is fully discussed by Tom [7, pg. 16-17]. The entire cell is immersed in liquid nitrogen to cool the system. A capacitance pressure sensor (Keller America PAA-41X) measures the pressure of the gas as it enters the cell and is manually controlled to 50.05 mbar every time. The same current (105 mA) is applied for each sample using a precision voltage and current source (Keithley 2420 Sourcemeter). By using low (25%) and high (99.99%) enrichment samples along with various other concentrations of *para*-hydrogen, a calibration plot was generated using the voltages obtained. To obtain a lower concentration of *para*-hydrogen through the converter, different converter temperature settings are used, assuming that the enrichment matches thermodynamic predictions. Figure 1.6 shows a typical calibration curve obtained through this method. Two separate calibration slopes are applied for high *para*-hydrogen concentrations (>99.5%) and low *para*-hydrogen concentrations (<99.5%), due to the slight irregularity of the curve with higher concentrations.

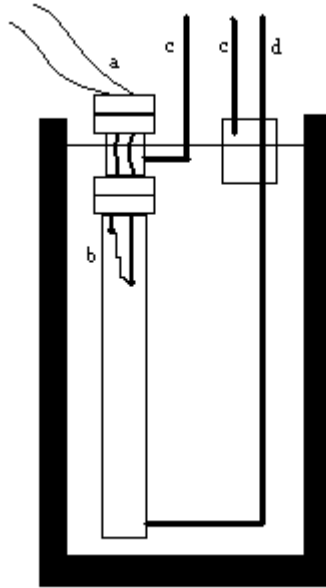


Figure 1.5: Schematic of the thermal conductance cell employed. (a): copper wires connected to the current source, (b): tungsten filament wire used to detect the change in voltage, (c): vacuum used to evacuate the cell, (d): sample gas line.

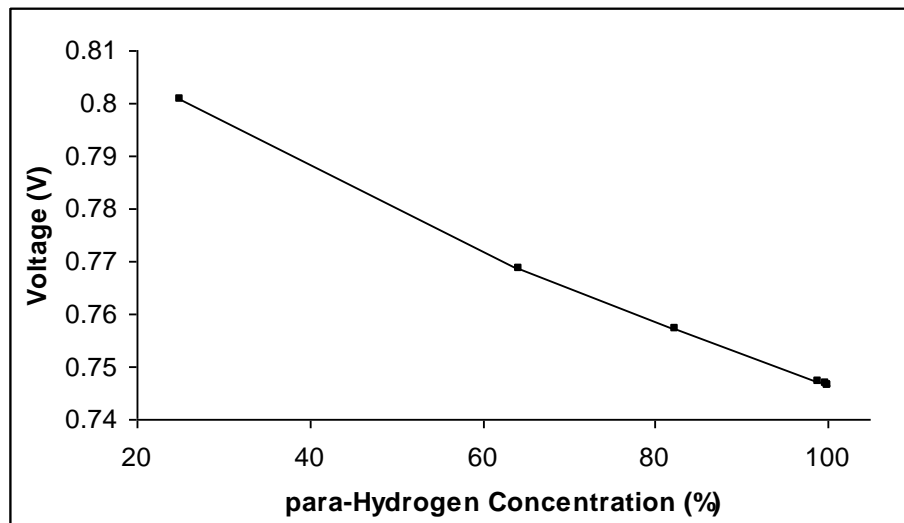


Figure 1.6: Plot of voltage reading against the known concentration of *para*-hydrogen.

Chapter 2

Refractive Index of Solid *para*-Hydrogen

2.1 Theory

Solid hydrogen is a true crystal where the molecules retain properties similar to those of free molecules. Solid hydrogens, including H₂, HD, and D₂, are dominated by quantum effects, the most important property being that the rotation of molecules is unhindered down to the lowest temperatures [15]. This is caused by the considerably larger intermolecular distance in solid *para*-hydrogen than other solids, such as neon [16]. The *para*-hydrogen crystal exists in a hexagonal close packed form, as determined by X-ray diffraction [17]. The rotational angular momentum, J , of each hydrogen molecule remains a valid quantum number in solid hydrogen due to the weak interaction of hydrogen molecules [15]. States with even quantum numbers are required to couple with $J = 0$ (*para*-) and states with odd quantum numbers are required to couple with $J = 1$ (*ortho*-), exclusively [18]. Because the quadrupole moment of *ortho*-hydrogen is slightly stronger than *para*-hydrogen, the concentration of *ortho*-hydrogen in a *para*-hydrogen crystal must be as low as possible. This ensures that molecules in the *para*-hydrogen crystal may be the least perturbed [18].

Solid *para*-hydrogen has become very useful in chemistry and physics, with particular emphasis in matrix isolation spectroscopy and the use as a medium for a Raman laser (described in Chapter 3). Matrix isolation spectroscopy in solid *para*-hydrogen has many advantages over other techniques for studying chemical reaction dynamics at low temperatures [18]. Previously, noble gases, such as neon and argon, have been used due to their weak perturbations and their lack of reactivity, making it possible to isolate chemically reactive species. However, the

interactions with the environment are significant, producing a broad linewidth that can hide most spectral information [16]. On the other hand, solid molecular *para*-hydrogen shows sharp linewidths that can resolve fine spectral structures originating from within the crystal [16]. Because molecules in *para*-hydrogen at 4.3 K occupy only a limited number of rotational levels, reactions in solid *para*-hydrogen can be considered state selective [19]. This property allows for the study of state dependent phenomena for a variety of reactions [18].

The present experiment was designed to determine the index of refraction of solid *para*-hydrogen in order to apply this knowledge with the theory of Raman scattering to produce a continuous wave (cw) Raman laser through solid *para*-hydrogen. Without an accurate value for the refractive index of solid *para*-hydrogen, the optical movement of light through the crystal cannot be fully understood. Our collaborators, Momose and Miyamoto, previously studied the refractive index of *para*-hydrogen at various wavelengths, but only at 6 K and with one polarization. One goal of this study is to duplicate their experiment and independently confirm their results. We would also like to understand how the index of refraction changes under different conditions. By varying the temperature of crystal production, we can observe the effect of different densities on the refractive index. By using different light sources, including visible and IR, we aim to understand how the refractive index changes with varying wavelengths. This is very important with the design of a Raman laser, as different wavelengths of light may be utilized in the future. Finally, we will look at the angle of polarization of IR light through the crystal to gain a further understanding for how a different polarization of light will have an effect on the refractive index.

2.2 Design

Three different lasers are used to achieve five different wavelengths of light. An argon ion laser (Coherent I90-5) produces the wavelengths 476, 496, and 514 nm, while a HeNe (Thorlabs HRP005S) emits 632 nm light. To also determine the refractive index with non-visible light, the HeNe was removed and replaced with an IR light source at 950 nm (Sacher Lasertechnik TEC 520 and MLD 1000). Before the light reaches the cryostat, both lasers are focused using two one meter focusing lenses (Thorlabs LA1464-B), combined using a beam splitter (Edmund Optics P45-076), and made collinear over ~5 feet. With both lasers collinear, two steering mirrors are used to create a beam path horizontally and vertically straight along the entire length of the optics table. A photodiode (Thorlabs DET 110), with an oscilloscope (Tektronix TDS1001B) to display the output, accurately measures the position of each laser to ensure the most precise alignment. Figure 2.1 shows a diagram of the optics configuration.

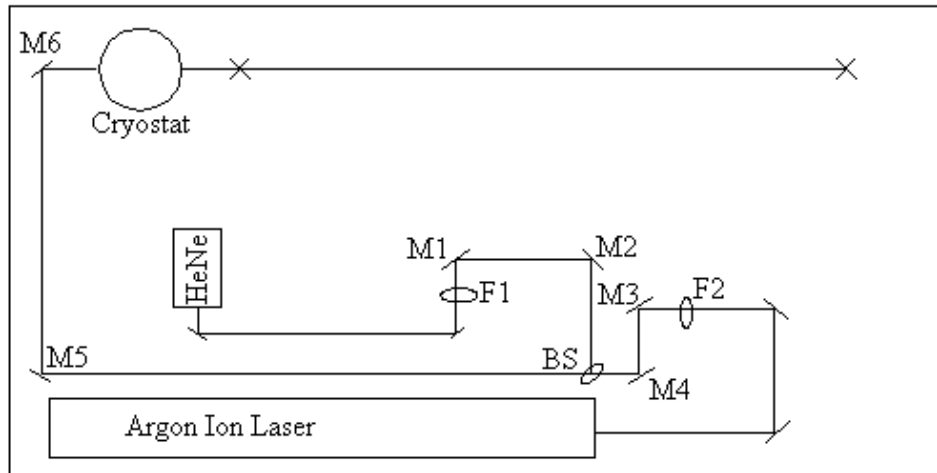


Figure 2.1: Diagram of optics alignment. M1/M2- steering mirrors for the HeNe, M3/M4- steering mirrors for the argon ion, M5/M6- steering mirrors for both lasers when collinear, F1/F2- one meter focusing lens for each laser, BS- beam splitter to combine the lasers, X- shows the locations of each reading using the photodiode detector.

The cryostat (Infrared Laboratories HD-3(8)) is designed to reach close to 4.3 K with minimal heat loss. A small stainless steel cell, where the solid hydrogen crystal is ultimately

produced, is coupled with the cold head of the cryostat. The cell has two glass windows sealing the openings. Indium gaskets are used to seal the windows to the cell [7, pg. 150]. One side is intentionally tilted with respect to the incident beam, illustrated in Figure 2.2. This tilt induces a deflection of the beam, allowing for the calculation of the refractive index of the solid hydrogen (explained in section 2.4). There are two glass windows on opposite sides of the cryostat to allow light to pass through. The same temperature controller (Lakeshore) previously used in the production of *para*-hydrogen is utilized here. Two temperature sensors are used, a germanium resistance thermometer (GRT), that displays the temperature of the actual cell, and a silicon diode sensor that measures the temperature of the cold head. The GRT will only operate properly below 100 K and is more accurate at low temperatures than the silicon diode. To set the temperature curves for each sensor, the toggles on the back of the temperature controller are set to “110” for the GRT and “101” for the silicon diode. To allow *para*-hydrogen to enter the cell, a line from the converter connects to the cryostat. *para*-Hydrogen is normally stored in the large Teflon tank and introduced to the cryostat from there. There is also a small storage tank connected between the cryostat and converter, which is used to store backing pressure during production of the crystal.



Figure 2.2: Illustration of the crystal cell. The light is input through the left side and vertically deflected by the tilted window as the light leaves the cell. The vertical deflection is directly related to the refractive index of the *para*-hydrogen crystal.

2.3 Crystal production

Before production of a crystal can begin, a few conditions must be fulfilled. The cryostat, inner sleeve, and hydrogen lines must be leak checked to a leak rate below $\sim 1 \times 10^{-10} \text{ L*atm*sec}^{-1}$ [7, pg. 151]. The argon ion and HeNe (Diode) lasers need to be collinear and run both vertically and horizontally straight through the cryostat and down the optics table. “Before” positions are obtained for comparison in the final calculations. The error limit on these measurements is ± 0.005 inches. If the height of the beam changes across the table by more than this limit, the beam is not considered “flat” and needs to be realigned. The light must be vertically aligned before introducing a crystal in order to produce accurate results.

The cooling process begins by filling the inner and outer dewars with liquid nitrogen until full. Throughout the experiment, the outer dewar should be refilled with liquid nitrogen as it evaporates. After a few hours, the temperature sensors should read about 77-78 K. Before the addition of liquid helium, the nitrogen must be purged from the inner dewar. A stopper with an input to allow gaseous nitrogen to enter and an output to allow liquid nitrogen to escape is utilized to help remove the liquid nitrogen. The pressure of the gaseous nitrogen is slowly raised to allow liquid to exit. The output liquid nitrogen can be recollected in a small dewar for reuse. To ensure the liquid is completely flushed, the operator should wait for the temperature of the cryostat to begin to slowly rise, and the liquid nitrogen to cease flowing from the output.

The next step involves cooling the cryostat with liquid helium to around 16 K, where the hydrogen will be entirely liquid. The set point for sensor B on the temperature controller is set to 16.000 K, with the heater setting turned to “Max.” Before beginning this process, it is recommended to have 80-90 psi of *para*-hydrogen stored in the large Teflon tank. Once the temperature of sensor B is below 40 K, the *para*-hydrogen is introduced into the cell. The phase

change to liquid will begin shortly with liquid collecting in the cell. It will take between 18-22 psi of *para*-hydrogen from the large Teflon tank to fill the cell. After the cell is full, the temperature of sensor B is slowly raised to boil off the liquid. This gas is collected in the small Teflon tank and stored for later use as backing pressure. Make sure the large Teflon tank full of *para*-hydrogen is closed off during this process. Between 200 - 300 psi of pressure is created and stored in the small tank. More *para*-hydrogen should be introduced into the cryostat with the temperature lowered to collect liquid hydrogen. Once the cell is filled with liquid hydrogen, the backing pressure is applied to the cell by opening the tank. The set point of the temperature is then slowly lowered to create a clean crystal. This procedure was adapted from Suzuki et. al. [20].

2.4 How to determine the index

Once the crystal is formed, the temperature set point should be lowered to 4.3 K. It will take 30 minutes to an hour for the temperature to reach 4.3 K and remain stable. At this point, the photodiode detector should be set at either the near or far position to begin readings. With the crystal in place, the light will be high on the far position and will require a lab jack or additional block to be placed under the detector. The height of this addition was measured to include in the final calculations. Measurements are taken using each wavelength at one place, then the detector moved to the other position and the position found for each wavelength again. Even though the horizontal position is not used in the calculation, it is recommended to take this reading along with the vertical to ensure the lasers have not translated horizontally. If different wavelengths are not horizontally aligned anymore, an optic may have been moved indicating that the light is no longer vertically aligned entering the cryostat. In order to find the center of the beam, the

detector is maximized and then moved until the signal on the oscilloscope has decreased a set amount. This is repeated on the other side of the maximum, and then averaged to find the center. This procedure is necessary due to the laser beam being larger than the detector. The decrease in signal is not a set value, but it must be the same on both sides of the maximum. After completing the values for a single temperature, the crystal must be melted to a liquid and re-cooled to a different temperature. If the temperature is raised with the crystal kept solid, the crystal will maintain the same number density as the lowest temperature obtained. This will not give a true understanding of how the density affects the refractive index. To vary the angle of polarization, a zero-order half-wave plate, centered at 1064 nm, is inserted immediately before the cryostat, and varied through different polarizations.

The vertical deflection of the beam is calculated using Equation 2.1,

$$\text{Height of block} + \text{Near measurement} - \text{Far measurement} = \text{Vertical Deflection} \quad (2.1)$$

where the height of the block refers to the block placed under the far detector. The full derivation used to determine the refractive index equation is shown in Appendix A. The equation,

$$\sin^{-1}\left[\frac{n_v}{n_c} \times \sin(90 - \theta_p)\right] = \sin^{-1}\left[\frac{n_v}{n_c} \times \sin\left[\sin^{-1}\left[\frac{n_a}{n_v} \times \sin \theta_6\right] + 90 - \theta_a\right]\right] + \theta_a - \theta_p \quad (2.2)$$

uses angle of the first window (θ_p), the angle of the table that the cell is mounted on (θ_t), the angle of the tilted window (θ_a), and the index of refraction of vacuum, air, and the unknown sample (n_v , n_a , n_u). θ_6 represents the angle of the light as it exits the crystal. It is determined by finding the vertical position of the light at two distances outside the cryostat. Equation 2.3 is then applied, where “D” is the distance between detector readings and “H” is the vertical deflection, found using Equation 2.1.

$$\theta_6 = \tan^{-1}(H/D) \quad (2.3)$$

In order to determine the unknown index of refraction, θ_p , θ_t , and θ_a must first be determined experimentally. Figure 2.3 illustrates the position of these three angles. The window on the far left was designed to be perpendicular to the incoming light, but the small angle of the table has introduced a slight deflection by this window. Without this angle, the first window would have no impact on the vertical displacement of the light. To determine these angles, the back reflection from each window is used. Figure 2.4 shows the relationship between the angle of the window, and the angle of the back reflection. The angle of the back reflection is determined by finding the height of the incoming light and the height of the back reflection at the same distance from the window.

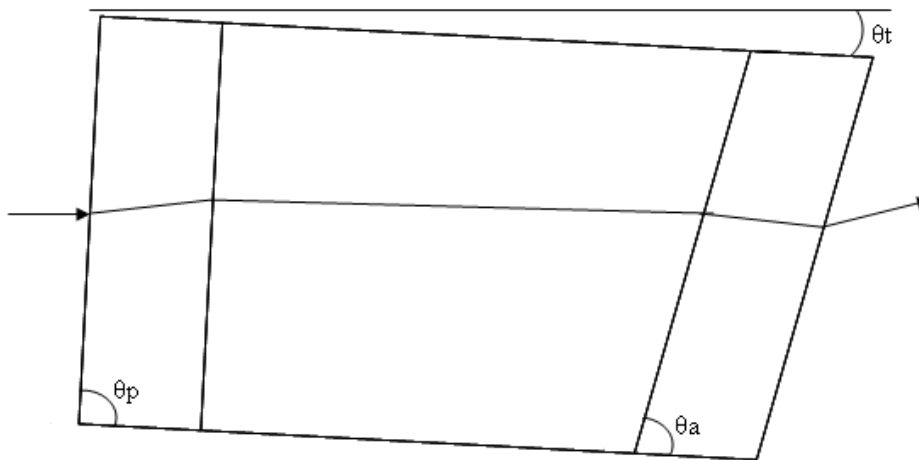


Figure 2.3: Illustration of the cell with the experimentally determined angles θ_t , θ_p , and θ_a labeled.

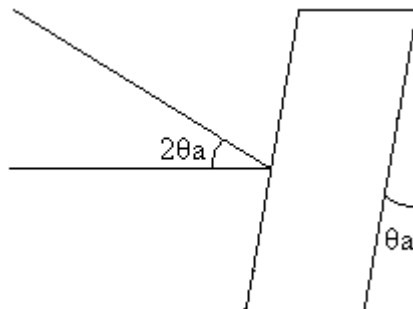


Figure 2.4: Illustration of the back reflection and the relationship with the angle of the window.

2.5 Results

Throughout this experiment, the refractive index of solid *para*-hydrogen was studied under numerous conditions: the growth rate of crystal, change in temperature (density), different wavelengths of light, and angle of polarization. At different wavelengths, slightly different values were observed but with a trend. The values for wavelengths 476 – 514.5 nm were within the same error limit, a decrease was seen as the wavelength increased. Figure 2.5 illustrates how the refractive index changed with different wavelengths of visible light. The graph also shows the data previously collected from our collaborator Momose, along with our new data. Figure 2.6 includes data collected at temperatures from 4.4 K to 10 K. By changing the temperature of the crystal, the density and crystal structure can be altered. By looking at the data, no significant change was observed as the temperature of the crystal was changed. This suggests that there was no change in the density or crystal structure within this data set.

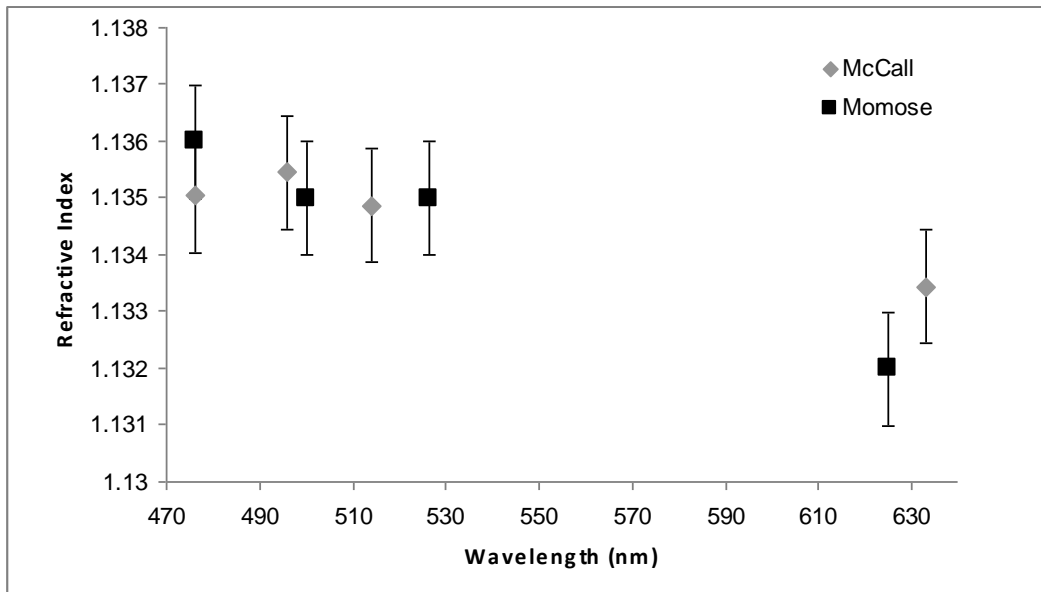


Figure 2.5: Plot of refractive index vs. wavelength of light at 6 K. Previous data from Momose is included.

	476 nm	496 nm	514 nm	633 nm
4.40 K	1.13473	1.13396	1.13284	1.13281
4.50 K	1.13426	1.13463	1.13367	1.13214
4.75 K	1.13468	1.13458	1.13408	1.13302
5.00 K	1.13481	1.13469	1.13418	1.13276
5.40 K	1.13462	1.135	1.13444	1.13276
6.00 K	1.13504	1.13546	1.13486	1.13343
7.00 K	1.1354	1.13355	1.13418	1.13323
7.50 K	1.13431	1.13531	1.13506	1.13333
10.00 K	1.13535	1.13463	1.13387	1.13307

Figure 2.6: Table of collected data including different wavelengths of light and different crystal temperatures.

Next, different methods were used to form a crystal. The same backing pressure was consistently used, and the crystal was grown passing through the triple point. When a crystal was originally formed, the temperature was dropped to 4.4 K within five minutes and immediate crystal growth was observed (fast growth crystal). However, to compare with Momose's method of growth, the crystal temperature was slowly dropped to 4.4 K over a one hour period of time (slow growth crystal). Figure 2.7 shows a comparison of data collected at 4.4 K with different methods of growing a crystal.

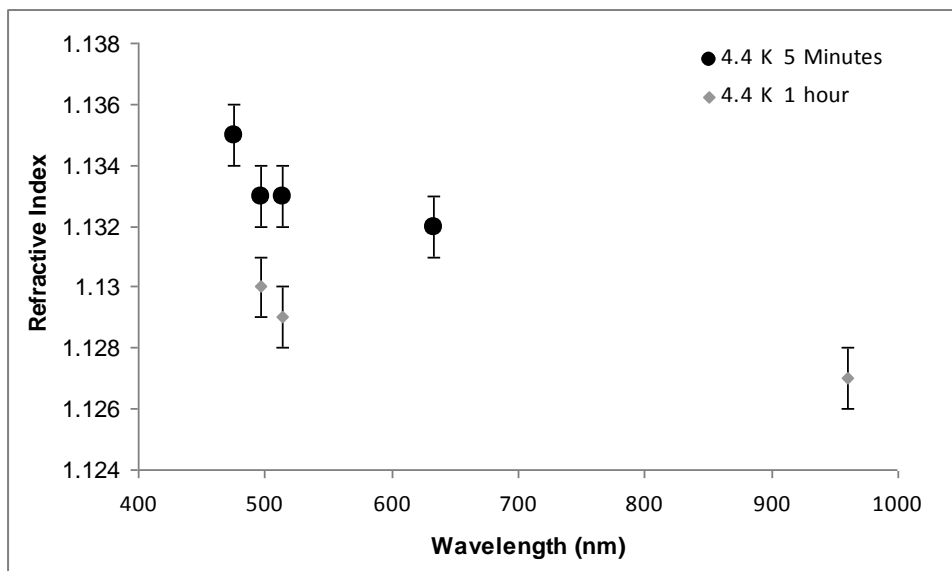


Figure 2.7: A comparison of growth methods on a plot of refractive index vs. wavelength of light.

To understand the effect of the polarization of light on the refractive index, the polarization of the IR light was varied using a zero-order half-wave plate, centered at 1064 nm. Figure 2.8 displays the change of the refractive index as the angle of polarization is varied.

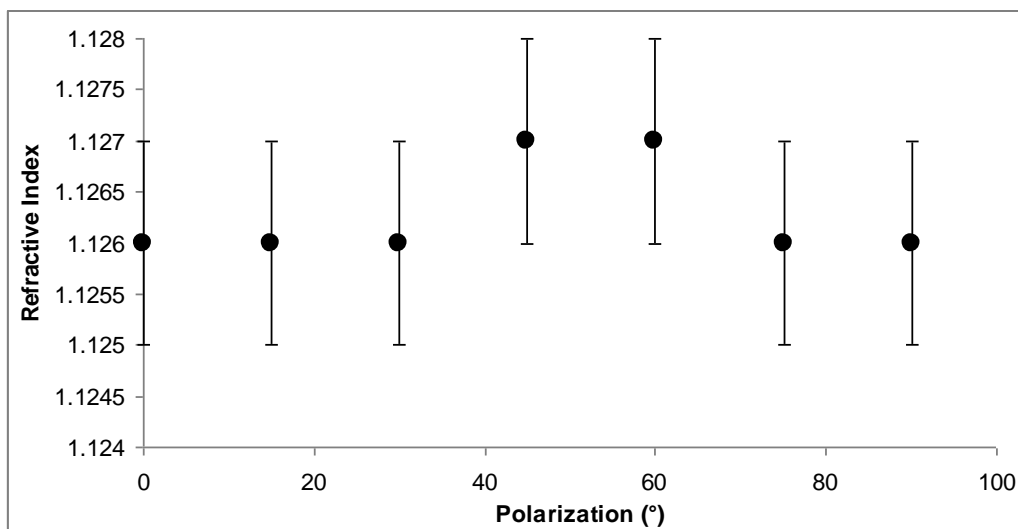


Figure 2.8: Plot of refractive index vs. polarization angle. The IR light was used with the 4.4 K crystal grown over an hour to collect this data.

2.6 Discussion

This experiment went through many modifications prior to completion. Issues arose with the cryostat not reaching 4.4 K, crystals were grown with obvious contaminants, and numerous other issues slowed down this experiment. The cryostat was modified to reach 4.4 K by increasing surface contact with the addition of indium foil as a spacer, reducing room radiation with radiation baffles inside the cryostat, and improving the heat switch mechanism. Crystals were growth with black impurities and cracks. If there was a leak in the hydrogen line, condensation appeared on the windows of the cells.

Previously, our collaborators Momose and Miyamoto conducted experiments to study the refractive index of solid *para*-hydrogen. One main motivation behind this project was to independently duplicate their data with a more precise means of measurement. A photodiode

detector was used to evaluate the vertical deflection of the light as it exited the cryostat. Also, we used the back reflection of the angled window to evaluate the angle of the tilted window. However, the desire to further understand how different variables affect the refractive index drove us to look at different wavelengths, temperatures, and angles of polarization.

To further understand our results, it is helpful to understand the crystal structure of solid *para*-hydrogen. A change in structure could have an impact on the refractive index because the medium is no longer the same. Solid hydrogen can exist as either hcp (hexagonal close-packed) or fcc (face-centered cubic) [21]. At low temperatures, an *ortho*-hydrogen fraction greater than 0.55 is generally required to form the ordered fcc structure, so we will be working mainly with the hcp structure.

Our original method of growing crystals involved dropping the temperature to 4.4 K and producing a crystal within five minutes. While we did observe clear crystals without any visible deformities, we noticed a discrepancy between the suggested method of growth in the literature and our method [21]. Concerns arose that by quickly dropping the temperature the crystal may not originate from one point of crystallization. Multiple points of crystallization may result in a non uniform hcp structure and possibly impact our measurements. To become more consistent with the literature, we attempted to grow a crystal over an hour by slowly lowering the temperature. We did not notice any significant change in the appearance of the crystal, but different results were obtained using this crystal. As shown in Figure 2.7, the values obtained for slow growth crystal were ~ 0.04 lower (error limit 0.01) than the values obtained for the fast growth crystal. These results are still under evaluation as we finish determining the angle of the slanted using the back reflection procedure (described in Section 2.4). This suggests a change in

the crystal structure as the crystal is produced at different rates and could be further studied by altering the growth rate and observing a change in refractive index.

When we initially sought to observe a *para*-hydrogen crystal at temperatures above 4.4 K, the crystal was produced at 4.4 K before increasing the temperature to higher values. By studying the data in Figure 2.6, it became evident that the refractive index was not changing (within the error limit) as the temperature increased. This results directly from our method of obtaining higher temperature crystals. By first creating a 4.4 K crystal, the entire cell is filled. The density of the crystal, and the structure, is unchanged as the temperature increases because there is not room in the cell for the molecules to rearrange with the high backing pressure applied. Thus, when we took measurements at different temperatures, we actually took measurements for the density of a 4.4 K crystal.

There was a trend observed with the refractive index from visible to IR wavelengths, as shown in Figure 2.7. This is consistent with Momose's previous data set. The same trend is also observed for both slow growth and fast growth crystals. There is a large gap from the highest visible wavelength studied to the IR light, due to our lack of light sources in this region. A future project to study more points within this region and deeper into the IR would help understand our current trend.

By varying the angle of polarization of the IR light, the change in refractive index was within our error limits (Figure 2.8). However, a slight increase was seen at 45° and 60°. As the half-wave plate is varied, the IR light is linearly vertically polarized at 0° and 90°, while it is horizontally polarized at 45°. Because the half-wave plate used was designed for 1064 nm light, there may have been a retardation effect seen in our results. To fully understand the effect of the

angle of polarization on the refractive index, a new half-wave plate and polarization optics may be utilized. This will give more precise measurements of the changing angle.

While we have inconclusive results of the effects of a change in temperature and angle of polarization on the refractive index, we have gained further knowledge about the growth of *para*-hydrogen crystals and a value for the refractive index at 4.4 K for visible and IR light.

Chapter 3

Design of a Raman Laser

3.1 Theory

The mid-infrared (mid-IR) spectral range of $900 - 2300 \text{ cm}^{-1}$ ($4.3 - 11 \text{ }\mu\text{m}$) provides access to characteristic molecular vibrations of organic molecules, such as carbonyl and cyano groups [22]. However, there are currently no convenient laser sources to cover the entire mid-IR spectral range. Of the sources available in this range, the long-wavelength cutoff is from $4.0 - 4.9 \text{ }\mu\text{m}$. Only a few sources provide coverage further into the mid-IR range, including different diode lasers, but with a weak output power [22]. Another current option to obtain mid-IR light is through an optical parametric oscillator (OPO) or difference frequency generation (DFG) device built in the laboratory. While an OPO or DFG device operating at $3 - 19 \text{ }\mu\text{m}$ can cover the entire mid-IR spectral range, the extreme difficulty and precision required to build and operate each device has resulted in rare usage for spectroscopic experiments [23]. In fact, there has never been a cw OPO or DFG produced beyond $\sim 5 \text{ }\mu\text{m}$.

Raman scattering occurs when a photon interacts with a molecule and becomes inelastically scattered. The red-shifted photon is generated as a result of the conservation of energy as the excitation of the molecule occurs. Stimulated Raman Scattering (SRS) is a combination of the theories of Raman scattering and stimulated emission. SRS produces frequency shifted outputs, where the difference between the Raman light frequency and the frequency of the pump light occurs at (or at multiples of) the strongest known Raman shifts [24]. Figure 3.1 shows an illustration of the Raman scattering process. Previously, SRS has been utilized in the cw regime to make cw Raman lasers [26]. However, due to the lower intensity of

cw pump lasers, these lasers need to operate near a molecular resonance to increase the Raman gain, resulting in the ability to tune over only very narrow regions of resonance. Another option for SRS is to generate infrared radiation in a single-pass gaseous Raman cell, but pump powers of more than 500 MW are required [27].

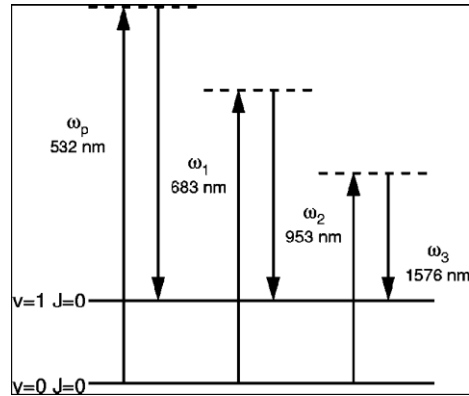


Figure 3.1: Illustration of the energy level diagram for the SRS process with the different Stokes frequencies labeled [25].

To solve some previous issues with SRS, hydrogen gas was introduced as a Raman gain medium. For a fiber ($\text{Yb}^{3+}/\text{Er}^{3+}$) material, the Raman shift is $\sim 440 \text{ cm}^{-1}$. However, the Raman shift in hydrogen gas is 4155 cm^{-1} , allowing for a greater shift in wavelengths when applied [26]. Another advantage of hydrogen gas is the relatively high Raman gain. Brasseur *et. al.* were able to successfully use hydrogen gas to create a cw Raman laser with a 35% conversion efficiency, and a threshold of pump power of 2 mW [26]. This is a significant improvement over previous gain media where a pump power of 10 – 100 MW was generally required to produce SRS [28].

Next, efforts were made to increase the Raman gain while using SRS. The gain of the SRS effect may be written as

$$G \propto \frac{n\alpha^2}{\lambda_s \Gamma} \quad (3.1)$$

where G represents the gain, n is the number density of the medium, α is the Raman polarizability, λ_s represents the wavelength of the Raman signal, and Γ is the width of the Raman transition [29]. Solid *para*-hydrogen has a larger number density ($\sim 2.6 \times 10^{22} \text{ cm}^{-3}$) and a smaller Raman line width of $\sim 7 \text{ MHz}$ than both gaseous and liquid *para*-hydrogen [30]. This line width is more than a factor of 10 times smaller than the narrowest line width achieved through a gaseous Raman-shifting medium [31]. Based on the relationships in Equation 3.1, solid *para*-hydrogen results in a larger SRS gain when used as the Raman-shifting medium. The $Q_1(0)$ Raman transition ($\nu = 1 \leftarrow 0, J = 0 \leftarrow 0$) produces a Raman shift of 4149.7 cm^{-1} . Figure 3.2 shows the energy level diagram for this transition.

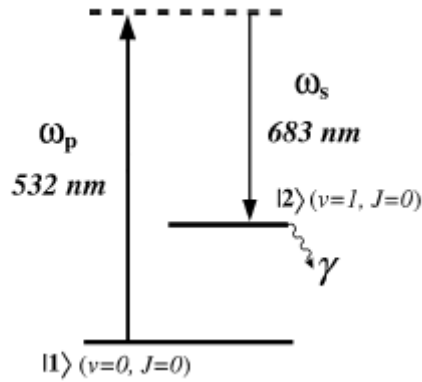


Figure 3.2: Energy level diagram of the $Q_1(0)$ Raman transition [32].

Because the electronic states are more than $90,000 \text{ cm}^{-1}$ above the ground state, the intermediate states are far detuned from resonances [33]. The gain coefficient for this transition through gas phase hydrogen ranges from $2.5 - 6.6 \times 10^{-3} \text{ cm/MW}$ depending on the wavelength [34]. On the other hand, solid *para*-hydrogen produces a gain of $18 \pm 3 \text{ cm/MW}$, a value about 7000 times greater than the gain coefficient for gas phase hydrogen [32].

An effective way to increase the conversion efficiency and power output is to utilize a basic laser resonant cavity in the set-up. This cavity is similar to a Fabry-Perot interferometer, consisting of two high reflectivity mirrors on either side of the gain medium. The Fabry-Perot

interferometer has a mechanically varied gap between the two mirrors, known as an etalon [35]. As this type of instrumentation is applied to SRS, cavities are built with a piezoelectric transducer (PZT) attached. A PZT can be attached to one of the mirrors or placed within the Raman cavity to adjust the cavity length. This allows the cavity to be scanned over multiple resonances until the Stokes output is visible [26]. By installing a cavity, the gain of the laser can be greatly increased. The single-pass gain of a Raman laser, G , is given in the following equation,

$$G = \frac{4\alpha P_p}{\lambda_p + \lambda_s} \tan^{-1}\left(\frac{l}{b}\right) \quad 3.2$$

where α is the Raman gain coefficient, λ_p and λ_s are the wavelengths of the pump and stokes beams, respectively, P_p is the power of the pump beam, l is the length of the gain medium, and b is the confocal parameter of the focused beam [36]. The Raman gain coefficient, α , has the following form,

$$\alpha = \frac{D(\nu_p - \nu_v)}{(\nu_i^2 - \nu_p^2)^2} = \frac{D\nu_s}{(\nu_i^2 - \nu_p^2)^2} \quad 3.3$$

where D is a constant incorporating the pressure and line width of the transition, ν_p and ν_s represent the frequency of the pump and Stokes beams, respectively, ν_i is the electronic frequency of the transition, and ν_v is the vibrational frequency of the transition [24, adapted from 32].

The reflectivity of the mirrors will increase the gain per pass in the cavity according to Equation 3.4,

$$G' = G \left(\frac{\sqrt{T_p}}{1 - \sqrt{R_p}} \right)^2 \quad 3.4$$

where G' is the increased gain, T_p is the transmission of the mirrors at the pump wavelength, and R_p is the reflectivity of the mirrors at the pump wavelength [37]. For example, if two mirrors are used with a reflectivity of 99.99% (0.01% transmission), the single-pass gain is increased by a factor of 40,000. To ensure that the gain is efficiently increased, the cavity must be doubly resonant at both the pump and Stokes wavelengths.

3.2 Requirements

With the refractive index of solid *para*-hydrogen in hand, we now aim to use this knowledge to design a SRS laser. Ultimately, we hope to design a cw laser to reach further into the mid-IR than current SRS lasers. This will involve the use of solid *para*-hydrogen as the Stokes medium and a cavity to increase the gain of our system. Before we begin work with IR light, we would like to test our theory and designs using a visible light source, an argon ion laser. When we input green light at 514.5 nm, the first order Stokes light will be red, at 654 nm. By using visible light, it will be easier to align the optics and verify the presence of SRS light.

To effectively produce Raman shifted light using a low power (a few mW) light source, we must be able to increase the gain of our system. To increase the gain, a high-finesse cavity (HFC) will be utilized. The most important part of an HFC is the finesse, which is determined by the reflectivity of the mirrors [38]. The finesse, F , is related to the reflectivity, R , by the Equation 3.5 [37].

$$F = \frac{\pi\sqrt{R}}{1-R} \quad 3.5$$

The finesse greatly increases as the reflectivity approaches 100%. For example, a mirror reflectivity of 99.99% produces a finesse of ~31,000, while a reflectivity of 99.9% results in a finesse of ~3100.

To achieve resonance between the pump laser and the cavity, the light must be both frequency locked and spatially mode matched to the cavity [26]. To achieve the frequency locking, a PZT is attached to one of the high reflectivity mirrors. This allows for the Raman cavity to be tuned through multiple resonances until the Stokes output is observed. To spatially mode match the pump laser to the cavity, the Rayleigh range of the input beam must match the Rayleigh range of the cavity [38]. This ensures that the beam is precisely centered in the cavity. The crystal is also placed in the middle of the cavity, so that the beam is centered in the middle of the Raman medium. The Rayleigh range is the distance from the waist of the beam to the cross section where the beam waist is doubled. The Rayleigh range, z_c , is given by Equation 3.6,

$$z_c = \frac{1}{2} [L(2R - L)]^{\frac{1}{2}} \quad 3.6$$

where L is the length of the cavity and R is the radius of curvature of the mirrors [39]. Having computed z_c for a given cavity, the next step is to match the Rayleigh range of the pump beam to the cavity value. Equation 3.7 calculates the Rayleigh range as the light, z_l , exits the laser,

$$z_l = \frac{2\pi w_0^2}{\lambda} \quad 3.7$$

where w_0 is half the diameter of the beam waist and λ is the wavelength of light. A focusing lens with focal length f can be placed to help match the Rayleigh range of the light to the cavity. By satisfying the following two equations (3.8 and 3.9), where d_1 is the distance from the light source to the lens and d_2 is the distance from the lens to the center of the cavity, the pump beam will be spatially mode matched to the cavity [38]. It is also important to align the back reflection off the first mirror to the input beam. The second mirror can be moved with a PZT to help center the beam, if necessary.

$$z_c = \frac{z_l f^2}{(f - d_1)^2 + z_l^2} \quad 3.8$$

$$d_2 = \frac{z_l^2 f + d_1^2 f - d_1 f^2}{(f - d_1)^2 + z_l^2} \quad 3.9$$

To ensure the cavity is stable, the following condition must be satisfied, where d is the distance between the two high reflectivity mirrors and R_1 and R_2 represent the radii of curvature of each mirror [37, pg. 428].

$$0 < \left(1 - \frac{d}{R_1}\right) \left(1 - \frac{d}{R_2}\right) < 1 \quad 3.10$$

If the cavity is not stable, a large amount of energy can escape the resonator on each pass.

Another method to help improve the finesse of a cavity is to minimize back reflection on surfaces within the cavity. In order to achieve this, Brewster's angle must be incorporated into these surfaces. If the angle of reflection and the angle of transmission added to 90° , the reflected wave would vanish completely [35]. By incorporating this fact into Snell's law, Brewster derived the Equation 3.11. By utilizing this theory into the design of the windows around the cell and cryostat, the reflection off these windows can be minimized.

$$\theta_B = \tan^{-1} \left(\frac{n_2}{n_1} \right) \quad 3.11$$

3.3 Initial Design

Figure 3.3 shows an illustration of the initial design for the solid *para*-hydrogen Raman laser. A faraday isolator (Newport ISO-04-532-MP) is necessary to prevent any feedback from being reflected back into the argon ion laser. Because light is being introduced into the cavity through the back of the first mirror, light will be able to bleed out through this mirror and travel

along the same path towards the laser. Without an isolator to act as a unidirectional valve for the light, the feedback may cause the laser to become unstable and change its output frequency.

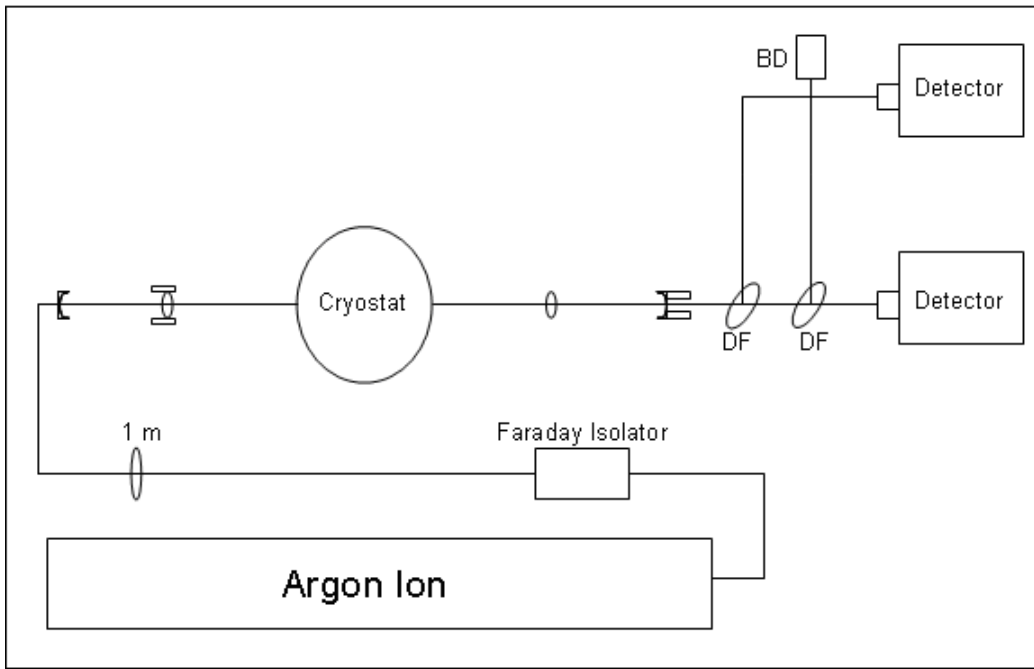


Figure 3.3: Optics design for Raman laser through solid *para*-hydrogen (not to scale).

A focusing lens must be used to focus the light into the center of the cavity. Roughly, a one meter focusing lens will need to be placed one meter from the center of the cavity. It is a good idea to apply the theory in Equations 3.6 – 3.9 when placing the lens to help achieve maximum output of Stokes light. After the cavity, it will be necessary to separate both beams to quantify the amount of light converted. A dichroic filter (labeled DF in the illustration) is a filter that features high reflectivity and high transmission ranges that are useful for beam separation. A filter (Edmund Optics NT67-074) will reflect 98% of light of wavelengths 490 – 554 nm and transmit 90% of light for 570 – 750 nm. By inserting two filters in a row, 99.96% of the pump beam will be separated from the Stokes beam. Additionally, 81% of the Stokes beam will also be transmitted through both filters, allowing for minimal power loss during this process. The pump beam reflected off of the second filter can be collected with a beam dump (labeled BD in Figure

3.3). Two detectors can be used to quantify the power simultaneously. Any power detector that is sensitive enough to measure light below one mW is sufficient.

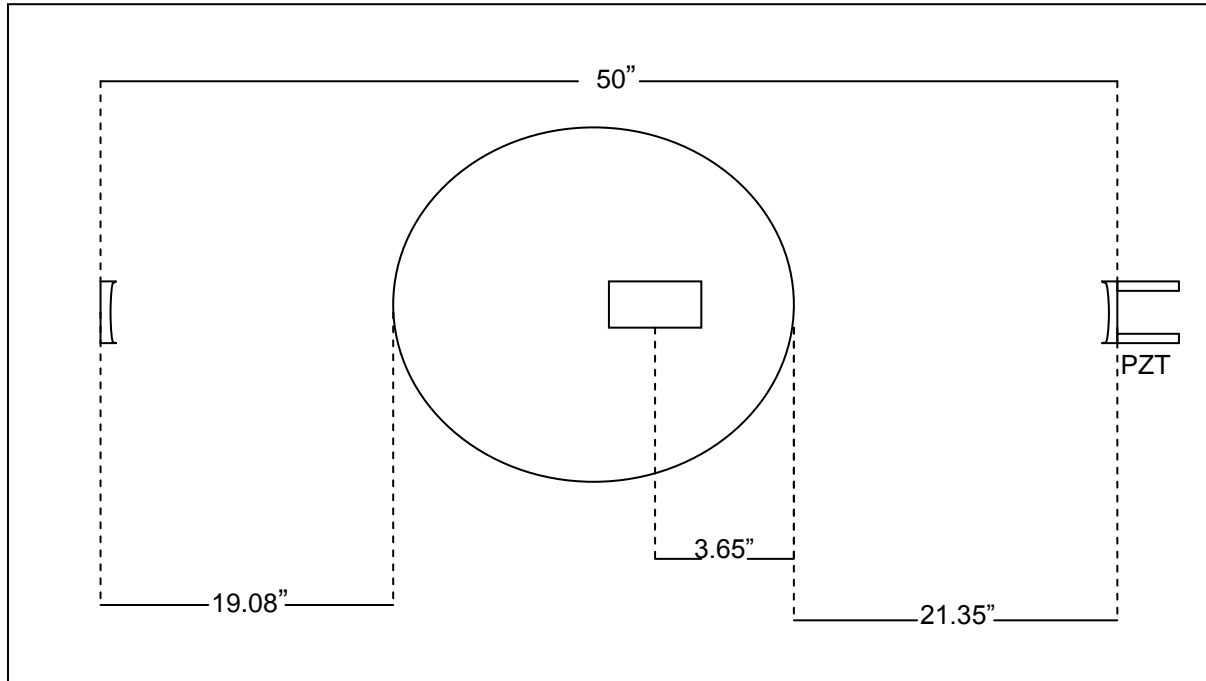


Figure 3.4: Close up view of the cavity around the cryostat (not to scale). Suggested distances are included based on the position of the crystal cell in the cryostat

Figure 3.4 shows an expanded view of the cavity around the *para*-hydrogen crystal. The most important part to this cavity is the two high reflectivity mirrors. First, the stability condition given in Equation 3.11 must be satisfied. As long as the distance between the two mirrors is less than the radius of curvature of both mirrors, this cavity will be stable. Due to the large size of the cryostat (ten inches across), a large cavity must be placed around it. A good starting estimate is 50 inches, which will allow room to place optics between the two mirrors. Thus, a radius of curvature of 1 m for both mirrors will be a good option. The mirrors must be concave to keep light contained within the same pathway. By polishing the outside of the mirrors where light is introduced, less power will be lost in this process. Lastly, the mirrors directly determine the finesse of the cavity based upon the reflectivity coating applied. For our purposes, we do not

need an extremely high finesse. This is due to the fact that solid *para*-hydrogen has a much larger gain than gas phase hydrogen. We are also initially testing a system with visible light and are not concerned with the quantity of conversion, but more with the ability to successfully produce SRS light. A lower finesse also allows for easier alignment of the system because it requires less precision to mode match the light to the cavity. On the other hand, we must also ensure that the finesse is sufficient to produce detectable light with our low power light source. A reflectivity of 99%, producing a finesse of 313, may be the best option for our cavity. However, power calculations should be performed before purchasing mirrors to confirm that enough power will be output to be detected. Ideally, the reflective coating will also cover both the pump and Stokes wavelengths of light. This will allow for sufficient build-up of power within the cavity.

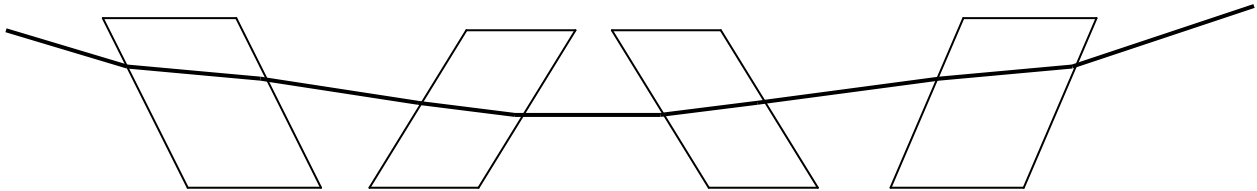


Figure 3.5: Diagram of beam path through cryostat (not to scale).

Brewster's angle must be incorporated into all the windows within the cavity, including the windows on the crystal cell and cryostat. Figure 3.5 shows a trace of the beam path as it travels through the cryostat. By using the indices of refraction found in the CRC [40], Brewster's angle was calculated for each surface. By applying these angles to each window, the windows on the outside of the cryostat must be tilted, and the windows on the hydrogen cell must be wedged to achieve all Brewster's angles. Appendix B shows a derivation of the angles required to design the windows at Brewster's angles. The angle of the input beam can be varied, along with the angle of each window.

The final addition to this cavity is a PZT device. When the second mirror is mounted with a PZT, the distance between the two mirrors can be varied to tune through the laser resonances in

the cavity. This method changed both the pump and Stokes beam path lengths by the same amount. However, it may be necessary to change the path length of each beam differently to achieve laser resonance. This may be achieved by placing two opposing Brewster's windows in the path of the light and change the optical path length using a Galvanometer. The index of refraction through a glass window is slightly changed by the wavelength of light, so path length will change differently for the pump and Stokes beam as they pass through these windows. By incorporating both of these means to alter the path length of the cavity, double resonance will be achieved and effective SRS will be possible.

3.4 Conclusion

In this section, I have presented the theory behind SRS, requirements to consider when creating the system, and an initial design of the optics and cavity. By presenting a fully explained guide, I hope to help lead my group members as they continue on with the Raman laser after I have left.

References

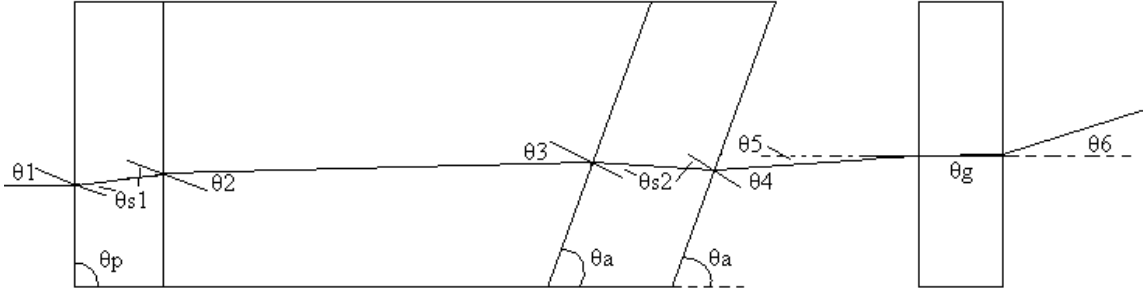
1. W. Heisenberg. *Z. f. Physik* **41**, 239 (1927).
2. K. F. Bonhoeffer and P. Harteck, *Naturwiss.* **17**, 182 (1929).
3. E. Wigner, *Z. f. Phys. Chem.* **23**, 28 (1933).
4. J. T. Kummer, *J. Phys. Chem.*, **66**, 9 (1962).
5. B. F. Minaev and H. Ågren, *J. Phys. Chem.* **99**, 21 (1995).
6. I. F. Silvera, *Rev. Mod. Phys.* **52**, 393 (1980).
7. B. A. Tom, *Nuclear Spin Dependence in Reactions of H_3^+ in the laboratory and the Interstellar Medium*, Ph.D. Thesis, University of Illinois Urbana-Champaign, (2009).
8. S. Tam and M. Fajardo, *Rev. Sci. Instrum.* **70**, 1926 (1999).
9. B. Tom, S. Bhasker, Y. Miyamoto, T. Momose, B. McCall, *Rev. Sci. Instrum.* **80**, 16108 (2009).
10. See EPAPS Document No. E-RSINAK-80-007902 for more detailed information about the *para*-hydrogen converter, thermal conductance, NMR, and solid hydrogen measurement techniques. For more information on EPAPS, see <http://www.aip.org/pubservs/epaps.html>.
11. Skoog, Holler, and Nieman. *Principles of Instrumental Analysis*. Thomson. (2005).
12. S. O. Kasap, *Principles of Electronic Materials and Devices, 2nd Ed.*, McGraw Hill, (2002).
13. A. Farkas, *Orthohydrogen, Parahydrogen, and Heavy Hydrogen*, Cambridge Univ. Press, London (1935).
14. A. T. Steward and G. L. Squires, *J. Scientific Inst.* **32**, 26 (1955).
15. J. V. Kranendonk, *Solid Hydrogen*. Plenum Press, New York, (1983).

16. T. Momose, H. Hoshina, M. Fushitani, and H. Katsuki, *Vib. Spec.* **34**, 95 (2004).
17. W. H. Keesom, J. de Smedt, and H. H. Mooy, *Proc. Kon. Akad. v. Wetens*, **33**, 814 (1930).
18. T. Momose, M. Fushitani, and H. Hoshina, *Int. Rev. in Phys. Chem.* **24**, 533 (2005).
19. M. Fushitani and T. Momose, *J. Chem. Phys.*, **120**, 1168 (2004).
20. M. Suzuki, M. Katsuragawa, R. S. D. Sihombing, J. Z. Li, and K. Hakuta, *Jour. Low Temp. Phys.*, **111**, 463 (1998).
21. P. C. Souers, *Hydrogen Properties for Fusion Energy*. Univ. of Cali. Press, California, (1986).
22. K. E. Kuyanov, T. Momose, and A. Vilesov, *App. Opt.* **43**, 6023 (2004).
23. K. L. Vodopyanov, *J. Opt. Soc. Am. B.* **16**, 1579 (1999).
24. G. Eckhardt, R. W. Hellwarth, F. J. McClung, S. E. Schwarz, and D. Weiner, *Phys. Rev. Letters*, **9**, 455 (1962).
25. B. J. McCall, A. J. Honeycutt, R. J. Saykally, C. M. Lindsay, T. Oka, M. Fushitani, Y. Miyamoto, and T. Momose, *Appl. Phys. Letters*. **82**, 1350 (2003).
26. J. K. Brasseur, K. S. Repasky, and J. L. Carlsten, *Opt. Letters*. **32**, 367 (1998).
27. M. Fushitani, S. Kuma, T. Miyamoto, H. Katsuki, T. Wakabayashi, T. Momose, and A. Vilesov, *Opt. Soc. of Am.* **28**, 37 (2003).
28. F. M Johnson, *Handbook of Lasers*. CRC, Ohio, (1971).
29. N. Bloembergen, *Nonlinear Optics*. Benjamin, New York, (1965).
30. T. Momose, D. P. Weliky, and T. Oka, *J. Mol. Spectrosc.* **153**, 760 (1992).
31. R. Sussman, T. Weber, E. Riedle, and H. J. Neusser, *Opt. Commun.* **88**, 408 (1992).
32. M. Katsuragawa and K. Hakuta, *Opt. Letters*, **25**, 177 (2000).

33. K. Hakuta, M. Suzuki, M. Katsuragawa, and J. Z. Li, *Phy. Rev. Letters*, **79**, 209 (1997).
34. W. K. Bischel and M. J. Dyer, *J. Opt. Soc. Am. B*, **3**, 677 (1986).
35. E. Hecht, *Optics*. Addison-Wesley, Mass, (1974).
36. P. Rabinowitz, A. Stein, R. Brickman, and A. Kaldor, *Opt. Letters*, **3**, 147 (1978).
37. E. Hecht, *Optics*. Addison-Wesley, Mass, (1987).
38. K. S. Repasky, L. E. Watson, and J. L. Carlsten, *App. Opt.* **34**, 2615 (1995).
39. H. Kogelnik and T. Li, *Handbook of Lasers*. CRC, Ohio, (1971).
40. *CRC Handbook of Chemistry and Physics, 90th Ed.*, <http://www.hbcnetbase.com/> (2010).

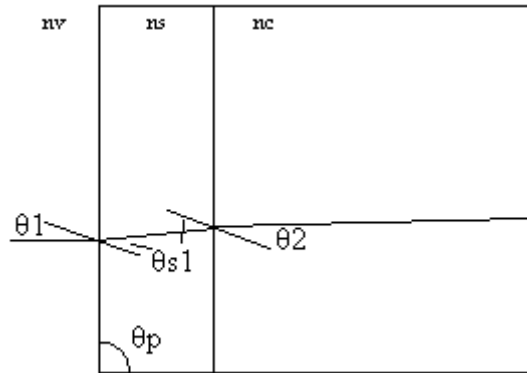
Appendix A

Refractive Index Derivation



To derive the necessary equation to determine the refractive index, the above figure of the cell and path of light is divided into three surfaces.

Surface 1:



$$n_v \times \sin \theta_1 = n_s \times \sin \theta_{s1}$$

$$n_s \times \sin \theta_{s1} = n_c \times \sin \theta_2$$

Combine the previous two equations

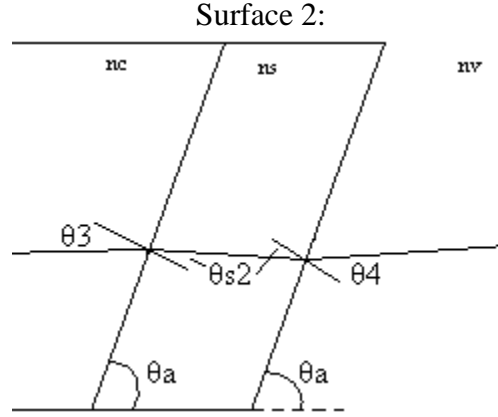
$$n_v \times \sin \theta_1 = n_c \times \sin \theta_2$$

Rearrange the equation

$$\theta_2 = \sin^{-1} \left[\frac{n_v}{n_c} \times \sin \theta_1 \right]$$

Using the relationship $\theta_1 = 90 - \theta_p$, where θ_p is the angle on the perpendicular window

$$\theta_2 = \sin^{-1} \left[\frac{n_v}{n_c} \times \sin(90 - \theta_p) \right] \quad (1)$$



$$n_c \times \sin \theta_3 = n_s \times \sin \theta_{s2}$$

$$n_s \times \sin \theta_{s2} = n_v \times \sin \theta_4$$

Combine the previous two equations

$$n_c \times \sin \theta_3 = n_v \times \sin \theta_4$$

Rearrange the equation

$$\theta_3 = \sin^{-1} \left[\frac{n_v}{n_c} \times \sin \theta_4 \right] \quad (2)$$

Using the relationship $\theta_3 = \theta_2 + \theta_p - \theta_a$, substitute into equation 2

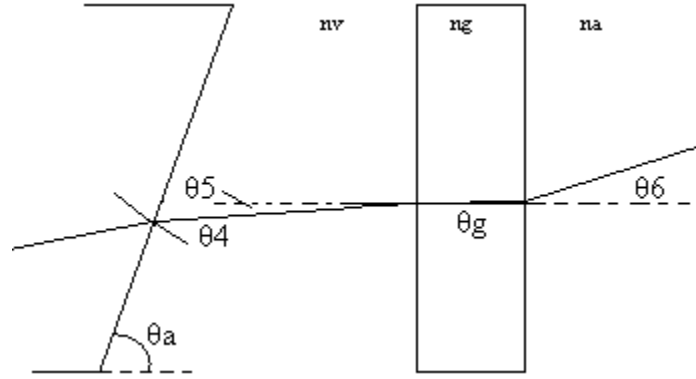
$$\theta_2 + \theta_p - \theta_a = \sin^{-1} \left[\frac{n_v}{n_c} \times \sin \theta_4 \right]$$

$$\theta_2 = \sin^{-1} \left[\frac{n_v}{n_c} \times \sin \theta_4 \right] + \theta_a - \theta_p \quad (3)$$

Setting equation 1 equal to equation 3

$$\sin^{-1} \left[\frac{n_v}{n_c} \times \sin(90 - \theta_p) \right] = \sin^{-1} \left[\frac{n_v}{n_c} \times \sin \theta_4 \right] + \theta_a - \theta_p \quad (4)$$

Surface 3:



$$n_v \times \sin \theta_5 = n_g \times \sin \theta_g$$

$$n_g \times \sin \theta_g = n_a \times \sin \theta_6$$

Combine the previous two equations

$$n_v \times \sin \theta_5 = n_a \times \sin \theta_6$$

Rearrange the equation

$$\theta_5 = \sin^{-1} \left[\frac{n_a}{n_v} \times \sin \theta_6 \right] \quad (5)$$

Using the relationship $\theta_5 = \theta_a + \theta_4 - 90$, substitute into equation 5

$$\theta_a + \theta_4 - 90 = \sin^{-1} \left[\frac{n_a}{n_v} \times \sin \theta_6 \right]$$

$$\theta_4 = \sin^{-1} \left[\frac{n_a}{n_v} \times \sin \theta_6 \right] + 90 - \theta_a \quad (6)$$

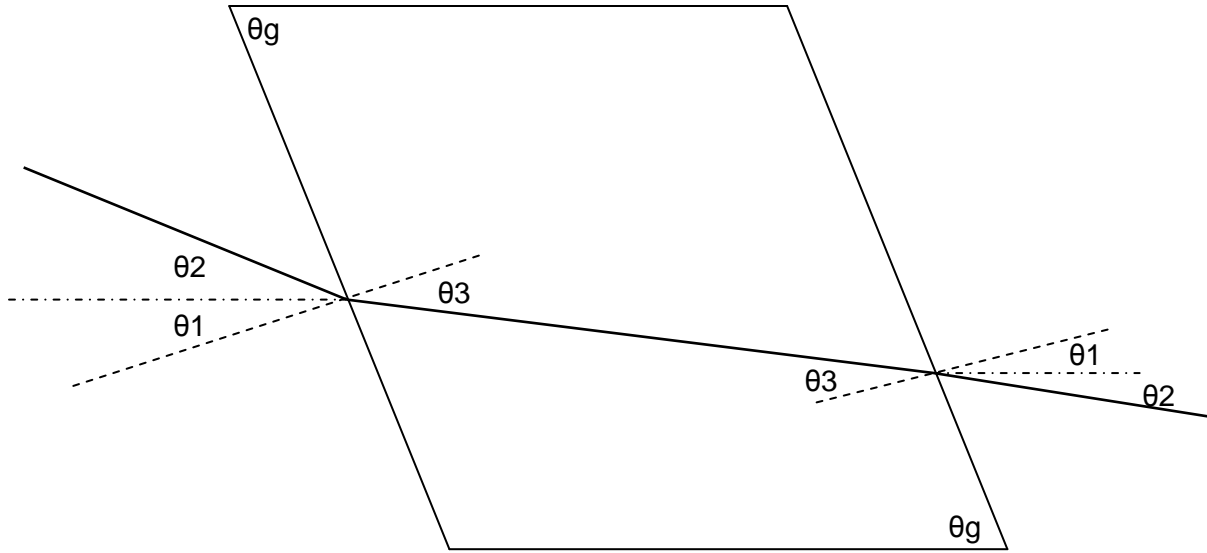
Substitute equation 6 into equation 4

$$\sin^{-1} \left[\frac{n_v}{n_c} \times \sin(90 - \theta_p) \right] = \sin^{-1} \left[\frac{n_v}{n_c} \times \sin \left[\sin^{-1} \left[\frac{n_a}{n_v} \times \sin \theta_6 \right] + 90 - \theta_a \right] \right] + \theta_a - \theta_p$$

Appendix B

Brewster's Angles

Window 1

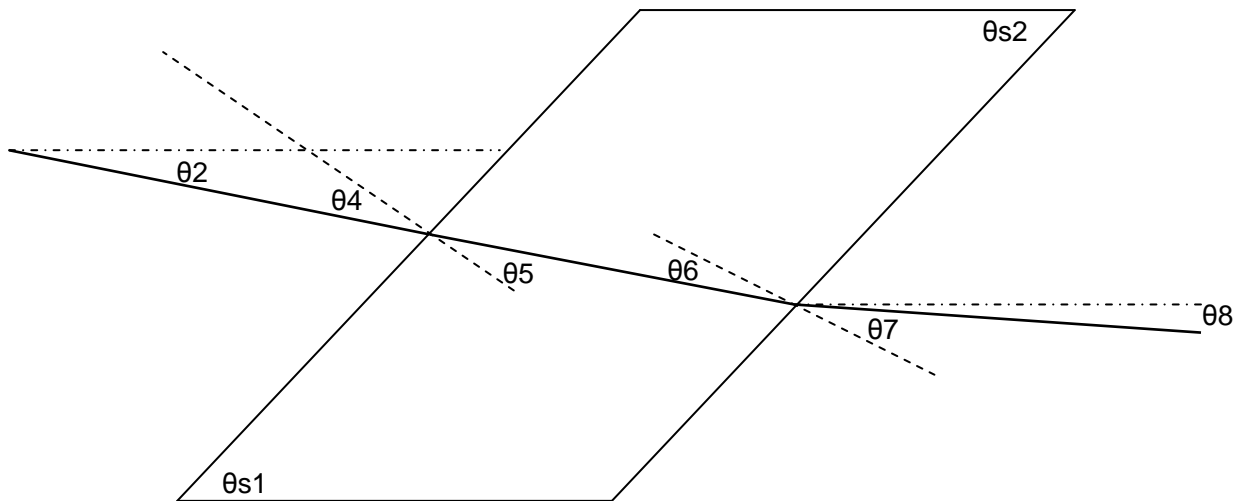


$$\theta_1 = 90 - \theta_g$$

$$\theta_1 + \theta_2 = 56.6$$

$$\theta_3 = 33.4$$

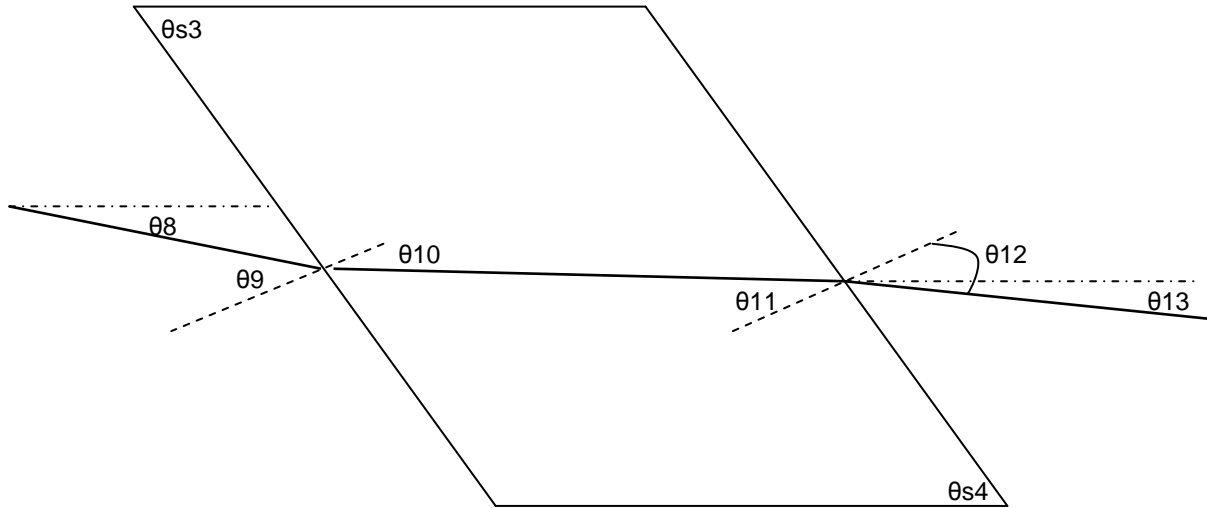
Window 2



$$\theta_2 + \theta_{s1} = 29.5$$

$$\theta_{s2} + \theta_8 = 32.6$$

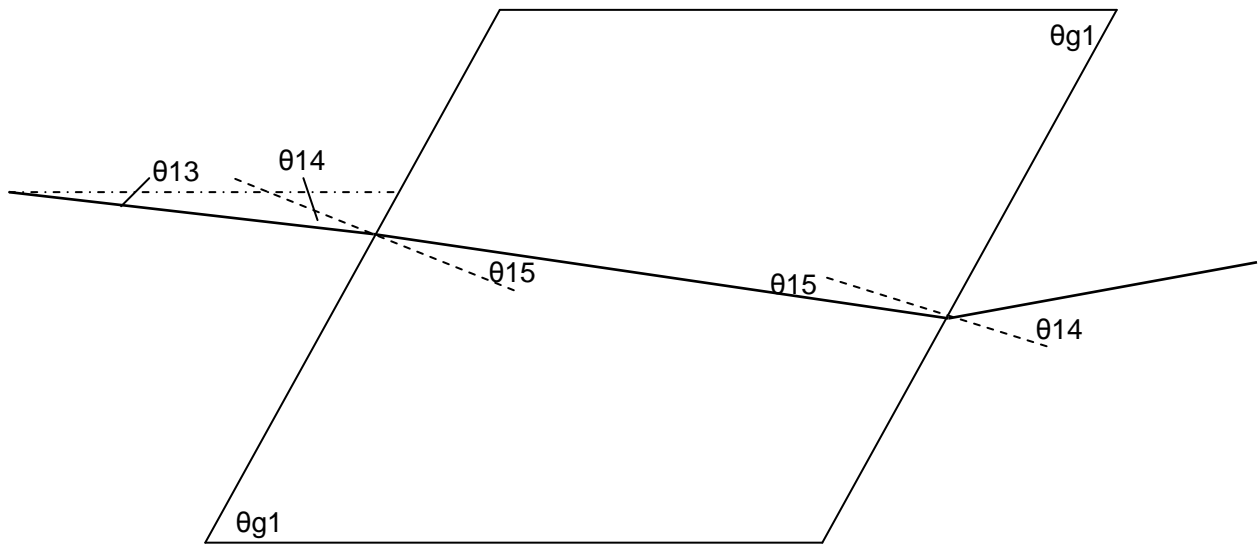
Window 3



$$\theta_{s3} - \theta_8 = 32.6$$

$$\theta_{s4} - \theta_{13} = 29.5$$

Window 4



$$\theta_{13} + \theta_{g2} = 33.4$$

Brewster's Angles:

$$\theta_1 + \theta_2 = 56.6^\circ, \theta_3 = 33.4^\circ, \theta_4 = 60.5^\circ, \theta_5 = 29.5^\circ, \theta_6 = 32.7^\circ, \theta_7 = 57.4^\circ$$

$$\theta_9 = 57.4^\circ, \theta_{10} = 32.7^\circ, \theta_{11} = 29.5^\circ, \theta_{12} = 60.5^\circ, \theta_{14} = 56.6^\circ, \theta_{15} = 33.4^\circ$$